Two-Directional Nodal Model for Co-Condensation Growth of Multicomponent Nanoparticles in Thermal Plasma Processing

Masaya Shigeta and Takayuki Watanabe

A more precise but easy-to-use model is developed and proposed to clarify nanoparticle growth with two-component co-condensation in thermal plasma processing. Computations performed for the molybdenum-silicon and titanium-silicon systems demonstrate that the model quantitatively estimates both the particle size distribution and the composition distribution of the silicide nanoparticles produced through co-condensation as well as nucleation and coagulation. The model also successfully obtains information that cannot be acquired by any other models. As a consequence, the detailed growth mechanisms of the silicide nanoparticles are eventually revealed. The present model is thus an "adaptable" and useful tool for analyzing nanoparticle growth processes, including co-condensation, with sufficient accuracy.

1. Introduction

1.1 Thermal-Plasma-Aided Nanoparticle Production

Thermal plasmas provide several distinctive advantages: high enthalpy, high chemical reactivity, variable properties, and steep temperature gradients. Additionally, thermofluid fields, such as temperature and velocity, are controllable by external electromagnetic fields (Ref 1-3). Hence, thermal plasma has been expected to be a potent tool for efficient production of nanoparticles. The production process starts from vaporization of raw materials, which is easily achieved by the remarkably high enthalpy of a plasma, even if the materials have high melting or boiling points. Subsequently, the vapor is transported to the tail or fringe of the plasma at high cooling rates, and the vapor becomes highly supersaturated. As a result, nanoparticles are rapidly generated through nucleation, condensation, and coagulation. Therefore, thermal plasma can be regarded as an innovative tool that automatically converts raw materials into nanoparticles.

Masaya Shigeta, Department of Mechanical Systems and Design, Graduate School of Engineering, Tohoku University, 6-6-01 Aramaki-Aoba, Aoba-ku, Sendai 980-8579, Japan; and **Takayuki Watanabe**, Department of Environmental Chemistry and Engineering, Interdisciplinary Graduate School of Science and Engineering, Tokyo Institute of Technology, 4259-G1-22 Nagatsuta, Midori-ku, Yokohama 226-8503, Japan. Contact e-mail: shigeta@fluid.mech.tohoku.ac.jp.

1.2 Nanoparticles of Silicides

Nanoparticles of silicides, e.g., $MoSi_2$ and $TiSi_2$, exhibit excellent mechanical strength, unique electrical properties, and high heat and oxidation resistance (Ref 4). Hence, silicide nanoparticles have been expected to be potentially useful materials for extremely small-scale electronic and mechanical applications such as electromagnetic shielding, solar control windows, gate materials for complementary metal-oxide semiconductors (CMOS), and contact materials in microelectronics. Silicide nanoparticles can also be fabricated by thermal plasmas, although the detailed formation mechanism has not yet been clarified.

Several experimental studies on silicide nanoparticle production by thermal plasmas have been conducted (Ref 5-9). However, only the characteristics of the products were evaluated because of measurement limitations. It is impossible to directly observe each and every process of the growth. Therefore, it is strongly expected that theoretical or numerical-modeling approaches will extract significant information that is unobtainable from experiments and will reveal the substantial mechanisms of silicide nanoparticle formation, including co-condensation processes of multicomponent vapors.

1.3 Modeling of Nanoparticle Formation in Thermal Plasma Processing

Nanoparticle formation in thermal plasma processing has been modeled for several decades, and the results indicate that the aerosol general dynamic equation can effectively describe that morphology (Ref 10-17). However, the computations have always required simplification because even the numerical solution is difficult to obtain due to its strong nonlinearity. For instance, the moment model, which can save computational time and resources,

often assumes a uni-modal log-normal particle size distribution (PSD) for mathematical closure (Ref 18). However, the PSD is known to deviate significantly from a log-normal distribution, especially in the early stage of nanoparticle formation. Although the modal aerosol dynamics model can treat a multimodal PSD, its mathematical formulation tends to be complicated (Ref 19). These models are usually used for numerical simulation of a particle-growth process with a simple condensation formula. In contrast, the discrete-sectional model can express any profile of PSD (Ref 20). However, it might also be difficult to be applied to multicomponent, co-condensation processes because of its sensitive dependency between the discrete regime and the sectional regime.

To overcome those problems, we developed another model for multicomponent nanoparticle formation involving co-condensation growth (Ref 9). The model can also handle any PSD by invoking the concept of the nodal discretization (Ref 21). In addition, the multicomponent, co-condensation regime was successfully described and calculated by a unique scheme considering a rarefied gas effect and the Kelvin effect. Consequently, the numerical results exhibited good agreement with the experiment results in the particle size and the composition of molybdenum/titanium-silicide nanoparticles. However, the model had to assume that all the same-size nanoparticles had the same composition, even though they actually had different compositions, because the coagulation process makes it complicated to estimate the compositions of nanoparticles.

Vorobev et al. also attempted to simulate the nanoparticle formation process with co-condensation growth by their own numerical approach (Ref 22, 23). They successfully predicted the two-dimensional distribution of tantalum-carbide nanoparticles fabricated by thermal plasma jets. However, several oversimplifications had to be adopted to obtain the solution. Because their model handles only the mean parameters, specific profiles of the PSDs cannot be determined.

The objective of this study is to develop and propose a more precise but easy-to-use model that can estimate both the PSD and the composition distribution of multicomponent nanoparticles produced through co-condensation as well as nucleation and coagulation. The model is constructed by improving the multicomponent co-condensation model in our previous work (Ref 9). This paper demonstrates several cases of computation to investigate how the present model predicts the nanoparticle growth processes in molybdenum-silicon and titanium-silicon systems. The validity of the model is discussed as well. In addition, the detailed mechanism of the metal-silicide nanoparticle formation is clarified through this modeling work.

2. Target

The target of this study is metal-silicide nanoparticle formation in thermal plasma processing at atmospheric
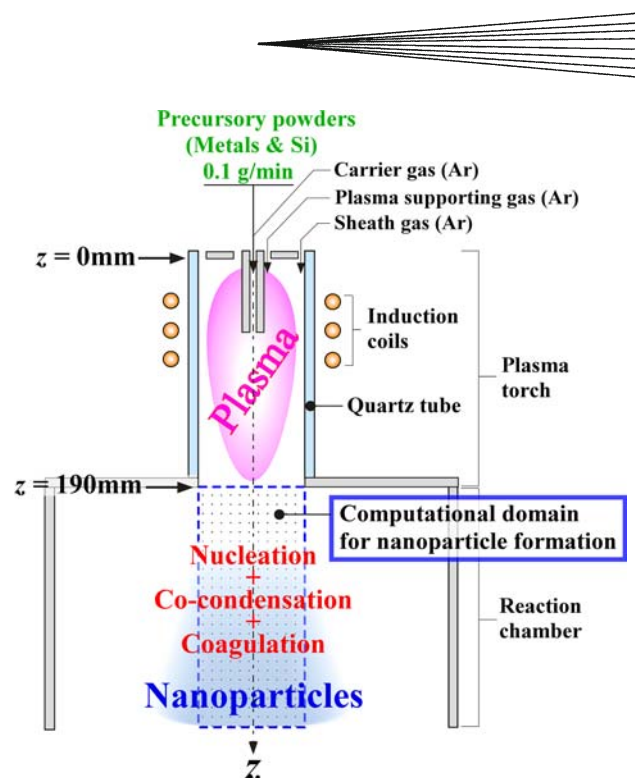

Fig. 1 Nanoparticle synthesis system using ITP

pressure, where the nanoparticles grow through co-condensation of metal vapor and silicon vapor. Figure 1 schematically illustrates a nanoparticle synthesis system aided by an induction thermal plasma (ITP). Compared with the other types of thermal plasmas such as a plasma jet, an ITP offers larger plasma volume and lower velocity, resulting in effective evaporation or reaction of materials by virtue of a longer residence time. In addition, an ITP is inherently contamination-free because it is generated without any internal electrodes. Therefore, an ITP can be regarded as the most reliable plasma for mass-producing nanoparticles with high purity.

The system consists of a plasma torch and a reaction chamber (Fig. 1). The plasma is induced by the radio-frequency electromagnetic field with an input power of 5.0 kW and an applied frequency of 4.0 MHz. From the top of the system, argon gas is injected as the carrier gas (1.0 Sl/min), the plasma supporting gas (3.0 Sl/min), and the sheath gas (30.0 Sl/min). These operating conditions are identical to those of the experiments (Ref 8, 9), so that the numerical results and the experiment results can be compared for model verification.

Premixed powders of metal and silicon are injected with the carrier gas from the injection tube as the precursors for silicide nanoparticles. The raw material powders are vaporized in the high-enthalpy field of the ITP. The material vapors are transported with the plasma flow to the reaction chamber in which the temperature drastically decreases (10^4-10^5 K/s). As a result, the material vapors become supersaturated, which leads to homogeneous nucleation. Once nuclei are generated, the vapors of the metal and silicon easily co-condense on the nuclei by heterogeneous condensation. This is the fundamental

mechanism of the metal-silicide nanoparticle formation. In addition, during that process, the nanoparticles collide, coagulate, and merge with each other. Such coagulation is also a considerable process in the growth of nanoparticles. To focus on the detailed mechanism of the metal-silicide nanoparticle formation, the region right below the plasma torch is selected as the present computational domain (Fig. 1).

The feed rate of the precursory powders is set to 0.1 g/min, which corresponds to 0.17% of the mass ratio to the injected argon gas. This can thus be regarded as a dilute condition where the effect of the precursory powders on the flow field is negligible. The initial silicon content in the precursory powders is chosen to be 66.7 at.%, which is the stoichiometric composition of metal disilicides. Our previous numerical study confirmed that the powders are completely vaporized in the plasma torch (Ref 9). Hence, the metal-silicon vapor concentrations corresponding to the initial condition are given at $z = 190$ mm, which is the inlet of the computational domain (Fig. 1).

Figure 2 depicts the thermofluid field of the bulk flow in the computational domain. The temperature and the velocity decrease monotonically, while the density increases. It is noted that these profiles were obtained from the two-dimensional axisymmetric distributions determined by the magnetohydrodynamics (MHD) approach in our previous study (Ref 9). The data in the computational domain were first averaged in the radial direction, and then the values were adapted for the axially finer grid system by linear interpolation. The present computation of the nanoparticle formation is conducted under this axially one-dimensional condition.

In the nanoparticle-formation process, nuclei are generated in advance, and then nanoparticles grow through co-condensation and coagulation. However, the nanoparticles will be solidified as the temperature continues to decrease. Once they are solidified, they cannot increase their diameters as sphere particles any more. They merely form their own aggregates. Indeed, several experimental studies reported that such products were observed in

metal-silicide nanoparticle synthesis by thermal plasmas as well (Ref 5, 6, 8). Since the present model handles only spherical particles, the computation is stopped when the temperature decreases to the solidifying point T_{sol}; the characteristics of the mature nanoparticles are then evaluated at this point.

However, the solidifying point actually depends on the metal/silicon ratio in each nanoparticle. In addition, it has been confirmed that the solidifying point of a particle smaller than 100 nm is lower than that of the bulk material (Ref 24). Those facts make it complicated and arduous to determine the variable solidifying points of the nanoparticles growing through co-condensation of the metal-silicon vapors and simultaneous coagulation between the nanoparticles. Therefore, in this study, the solidifying points are assumed to be identical to those of the disilicides that are obtained from the phase diagrams (Ref 25). That is, the solidifying point in the molybdenum-silicon system is set to T_{sol} (Mo-Si) = 1673 K, which corresponds to the axial position at $z = 238.37$ mm, while the solidifying point in the titanium-silicon system is T_{sol} (Ti-Si) = 1603 K, which corresponds to the axial position at $z = 241.00$ mm (Fig. 2).

3. Model Description

3.1 Concept and Assumptions

In general, more precise models are required for numerical analyses of any phenomena. Thus, the model formulation tends to be complicated, and the models often become difficult to handle. However, from an engineering viewpoint, even such models should be as easy as possible to use, while retaining their preciseness. Based on this concept, a new model is developed for numerically analyzing nanoparticle formation with multicomponent co-condensation.

The present model offers three major advantages: (I) it can express any profile of PSD; (II) it simultaneously estimates the size and composition of nanoparticles; and (III) the model formulation is arithmetic and straightforward, so the model itself is simple.

The model is formulated with the following assumptions: (a) nanoparticles are spherical; (b) nanoparticle inertia is negligible; (c) the velocity and temperature of nanoparticles are identical to those of the bulk flow; (d) heat generated by condensation is negligible; (e) electric charge of nanoparticles is also negligible; and (f) the material vapors are regarded as an ideal gas without chemical reactions.

3.2 Two-Directional Nodal Discretization

The PSD of an assembly of nanoparticles is always given as a function of the particle size. In our previous model, the PSD was discretized for the particle size by nodal approximation (Ref 9). In this study, the PSD is defined as a function of the composition as well as the particle size because the nanoparticles can contain both
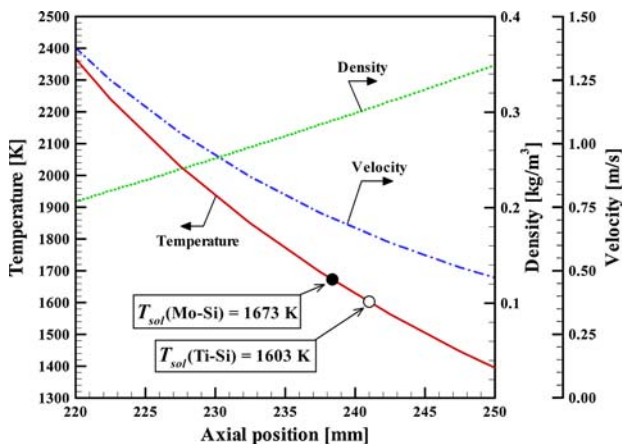

Fig. 2 Thermofluid field of bulk flow in computational domain

metal and silicon. Hence, the particle size-composition distribution (PSCD) is introduced in place of the PSD. PSCD is expressed by nodal discretization for the two individual directions of the particle size and the composition, where the nanoparticles reside only at the nodes as shown in Fig. 3(a-c).

The nodes are spaced linearly on a logarithmic scale in the size direction to cover the wide range of particle sizes.

$$v_{k+1} = f_v v_k \quad (k = 1, 2, \ldots, k_{max} - 1) \tag{Eq 1}$$

Here, v is the particle volume, and subscript k represents the node number in the size direction. The geometric spacing factor for size f_v and the number of nodes k_{max} are chosen to be 1.6 and 58. These values provide sufficient accuracy for the size range of the nanoparticles produced in thermal plasma processing. The particle volume at the first node is arbitrarily set to 10-mer of the material M:

$$v_1 = 10 v_M \tag{Eq 2}$$

where v_M is the volume of the monomer of material M. In this study, $M = 1$ corresponds to metal and $M = 2$ to silicon. In Eq 2, $M = 2$ is set in the present computation.

The nodes are linearly spaced in the composition direction.

$$x_{n+1} = x_n + \Delta x \quad (n = 1, 2, \ldots, n_{max} - 1) \tag{Eq 3}$$

Here, x is the content of material 2 in a particle, and the subscript n denotes the node number in the composition direction. The increment Δx is chosen to be 0.025, and the number of nodes n_{max} to be 41. The particles at the first node contain only material 1, while the composition of the particles at the n_{max}-th node is 100% material 2.

$$x_1 = 0 \tag{Eq 4}$$

$$x_{n_{max}} = 1 \tag{Eq 5}$$

3.3 Governing Equations

The formation of a nanoparticle assembly is described well by the general dynamic equation (GDE) for aerosol (Ref 24). Rewriting the GDE with the two-directional nodal approximation defined in Section 3.2, the particle concentration N at node (k, n) is given by

$$\frac{dN_{k,n}}{dt} = [\dot{N}_{k,n}]_{nucl} + [\dot{N}_{k,n}]_{coag} + [\dot{N}_{k,n}]_{cond} \tag{Eq 6}$$

where $[\dot{N}]$ represents the net production rate. The subscripts nucl, coag, and cond stand for the contributions from nucleation, coagulation, and condensation.

3.3.1 Nucleation Process. The algorithm of the nucleation process is illustrated in Fig. 3(a). The net production rate at node (k, n) due to nucleation is given as

$$[\dot{N}_{k,n}]_{nucl} = I_M \xi_{kM}^{(nucl)}. \tag{Eq 7}$$

When material 1 nucleates ($M = 1$), the k-th node in the first composition nodes ($n = 1$) obtains particles. When material 2 nucleates ($M = 2$), particles are supplied to the k-th node in the maximum composition nodes ($n = n_{max}$).
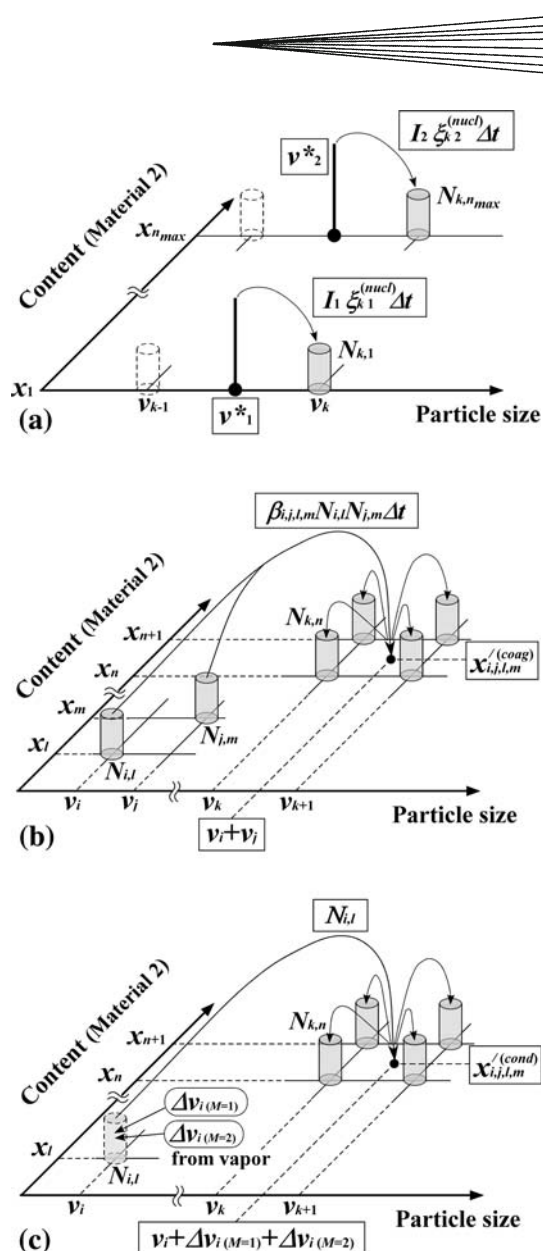

Fig. 3 Algorithm of nanoparticle formation: (a) Nucleation, (b) coagulation, and (c) co-condensation

I_M is the homogeneous nucleation rate of material M proposed by (Ref 26).

$$I_M = N_{S_M}^2 S_M \sqrt{\frac{2\sigma_M}{\pi m_M}} \exp\left(\Theta_M - \frac{4\Theta_M^3}{27(\ln S_M)^2}\right) \tag{Eq 8}$$

S_M is the supersaturation ratio of material M defined as the ratio of the vapor pressure to the saturation vapor pressure.

$$S_M = \frac{p_{vapor_M}}{p_{S_M}} = \frac{N_{vapor_M}}{N_{S_M}} \tag{Eq 9}$$

Here, p is the pressure. The subscripts vapor and S denote the vapor and the saturation state. Θ_M is the normalized surface tension of material M.

$$\Theta_M = \frac{\sigma_M s_M}{k_B T} \qquad \text{(Eq 10)}$$

Here, σ_M is the surface tension of material M, s_M is the surface area of the M monomer, k_B is the Boltzmann constant, and T is the temperature.

Table 1   Material properties used in the present study (Ref 30)

Material	Diameter of monomer, nm	Surface tension, N/m: $\sigma = \sigma_0 - (T - T_0)d\sigma/dT$		
		T_0	σ_0	$d\sigma/dT$
Mo	0.272	2880	2.25	0.00030
Ti	0.294	1958	1.65	0.00026
Si	0.234	1683	0.865	0.00013

Because a nucleus has a critical size due to the balance between growth and evaporation, a nucleus smaller than the critical size easily evaporates and cannot exist as a particle. Thus, only the next higher node can have embryos of particles (Fig. 3a). The size operator for nucleation of material M is introduced considering the conservation of the particle volume.

$$\xi_{kM}^{(\text{nucl})} = \begin{cases} \dfrac{v_M^*}{v_k}; & \text{if}\left(v_{k-1} < v_M^* < v_k\right) \\[2mm] \dfrac{v_M^*}{v_1}; & \text{if}\left(v_M^* < v_1\right) \\[2mm] 0; & \text{otherwise} \end{cases} \qquad \text{(Eq 11)}$$

The critical size of nucleus v_M^* is determined by both the material properties and the state of the vapor (e.g., the temperature and the saturation ratio) (Ref 24).
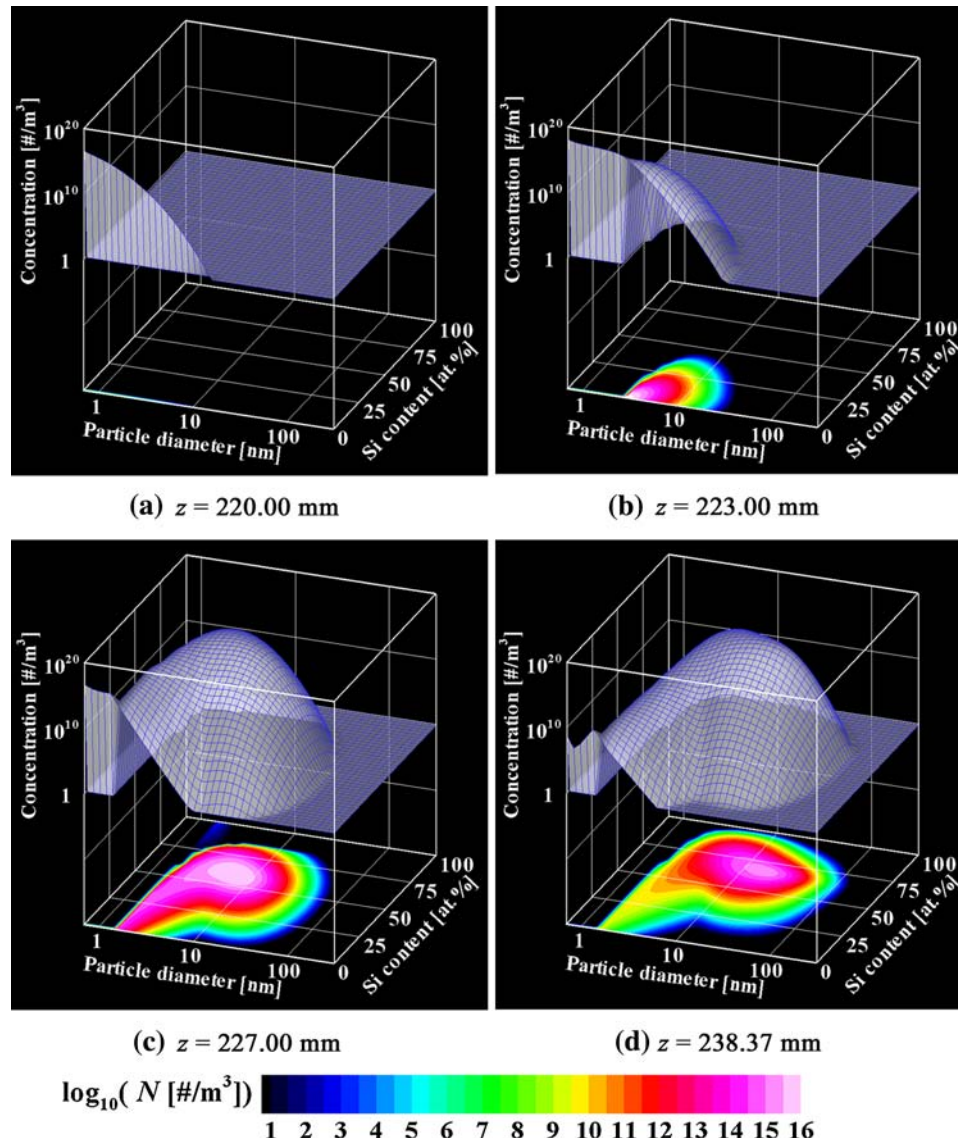

(a) $z = 220.00$ mm

(b) $z = 223.00$ mm

(c) $z = 227.00$ mm

(d) $z = 238.37$ mm

$\log_{10}(N\,[\#/\text{m}^3])$

1 2 3 4 5 6 7 8 9 10 11 12 13 14 15 16

Fig. 4   Nanoparticle growth process in Mo-Si system ($\alpha_{\text{Mo}} = \alpha_{\text{Si}} = 0.05$)

$$v_M^* = \frac{\pi}{6} \left(\frac{4\sigma_M v_M}{k_B T \ln S_M} \right)^3 \qquad \text{(Eq 12)}$$

3.3.2 Coagulation Process. Figure 3(b) depicts the algorithm of the coagulation process. The net production rate at node (k, n) due to coagulation of the particles is written as

$$[\dot{N}_{k,n}]_{\text{coag}} = \frac{1}{2} \sum_i \sum_j \sum_l \sum_m \xi_{i,j,k}^{(\text{coag})} \psi_{i,j,l,m,n}^{(\text{coag})} \beta_{i,j,l,m} N_{i,l} N_{j,m}$$
$$- N_{k,n} \sum_i \sum_l \beta_{i,k,l,m} N_{i,l} \qquad \text{(Eq 13)}$$

which is the Smoluchowski's equation modified with splitting operators for coagulation. Subscripts i and j denote the node numbers in the size direction, while the subscripts l and m denote those in the composition direction. The first term of the right-hand side expresses the particle gain at node (k, n) due to collisions between the particles at the other nodes. The second term of the right-hand side describes the particle loss at node (k, n) due to collisions between the particles at node (k, n) and the particles at the other nodes. Particles with volumes v_i and v_j collide and coagulate, and consequently form a new particle with the volume $v_i + v_j$. When the particle with v_i has the composition x_l and the particle with v_j has the composition x_m, the composition (the content of material 2) of the new particle is estimated to be

$$x_{i,j,l,m}^{\prime(\text{coag})} = \frac{v_i x_l + v_j x_m}{v_i + v_j}. \qquad \text{(Eq 14)}$$

The group of new particles is split into the adjacent nodes under the mass-conserving condition (Fig. 3b). Hence, the splitting operators in size direction ξ and in composition direction ψ are written as follows.

$$\xi_{i,j,k}^{(\text{coag})} = \begin{cases} \dfrac{v_{k+1} - (v_i + v_j)}{v_{k+1} - v_k}; & \text{if } (v_k < v_i + v_j < v_{k+1}) \\[2mm] \dfrac{(v_i + v_j) - v_{k-1}}{v_k - v_{k-1}}; & \text{if } (v_{k-1} < v_i + v_j < v_k) \\[2mm] 0; & \text{otherwise} \end{cases} \qquad \text{(Eq 15)}$$

$$\psi_{i,j,l,m,n}^{(\text{coag})} = \begin{cases} \dfrac{x_{n+1} - x_{i,j,l,m}^{\prime(\text{coag})}}{x_{n+1} - x_n}; & \text{if } \left(x_n < x_{i,j,l,m}^{\prime(\text{coag})} < x_{n+1} \right) \\[2mm] \dfrac{x_{i,j,l,m}^{\prime(\text{coag})} - x_{n-1}}{x_n - x_{n-1}}; & \text{if } \left(x_{n-1} < x_{i,j,l,m}^{\prime(\text{coag})} < x_n \right) \\[2mm] 0; & \text{otherwise} \end{cases} \qquad \text{(Eq 16)}$$

β in Eq 13 is the collision frequency function, which is often written in the form for a free molecular regime. However, in this study, the wide size range covers large particle diameters comparable to the gas mean free path.
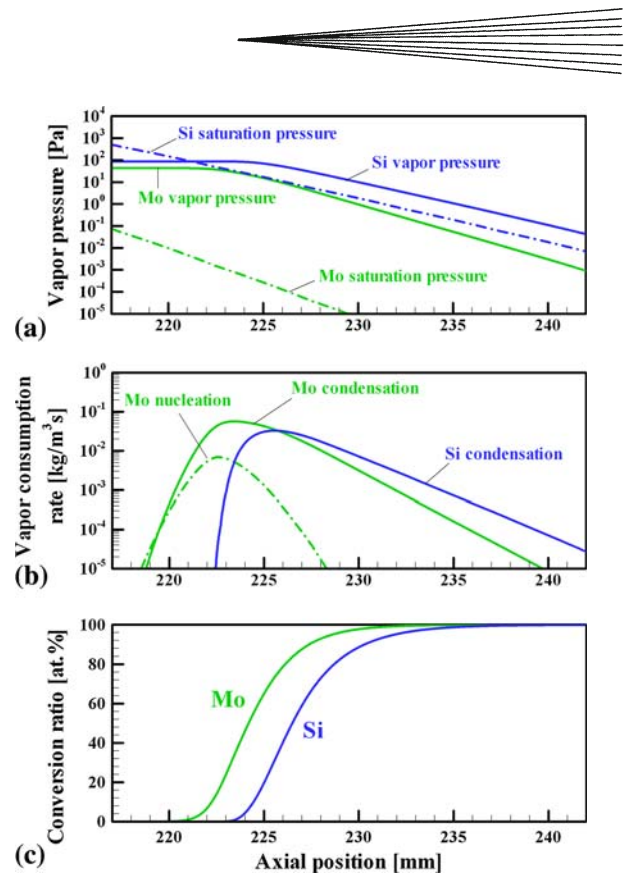

Fig. 5 Characteristics of vapor conversion in Mo-Si system ($\alpha_{\text{Mo}} = \alpha_{\text{Si}} = 0.05$): (a) Vapor pressure, (b) vapor consumption rate, and (c) conversion ratio

Thus, the Fuchs form of the collision frequency function is adopted (Ref 27).

$$\beta_{i,j,l,m} = 2\pi (D_i + D_j)(d_i + d_j)$$
$$\times \left[\frac{d_i + d_j}{d_i + d_j + 2\sqrt{g_{i,l}^2 + g_{j,m}^2}} + \frac{8(D_i + D_j)}{(d_i + d_j)\sqrt{\bar{c}_{i,l}^2 + \bar{c}_{j,m}^2}} \right]^{-1} \qquad \text{(Eq 17)}$$

$$g_{i,l} = \frac{\pi \bar{c}_{i,l}}{24 D_i d_i} \left\{ \left(d_i + \frac{8D_i}{\pi \bar{c}_{i,l}} \right)^3 - \left[d_i^2 + \left(\frac{8D_i}{\pi \bar{c}_{i,l}} \right)^2 \right]^{\frac{3}{2}} \right\} - d_i \qquad \text{(Eq 18)}$$

$$\bar{c}_{i,l} = \sqrt{\frac{8 k_B T}{\pi v_i \left[\rho_{(M=1)}(1 - x_l) + \rho_{(M=2)} x_l \right]}}. \qquad \text{(Eq 19)}$$

Here, d is the particle diameter, $\rho_{(M=1)}$ and $\rho_{(M=2)}$ are the densities of the materials 1 and 2, and the diffusion coefficient D of each particle is given by Ref 24, 28.

$$D_i = \frac{k_B T}{3\pi \mu d_i} \left\{ 1 + \text{Kn}_i \left[A_1 + A_2 \exp\left(-\frac{2A_3}{\text{Kn}_i} \right) \right] \right\} \qquad \text{(Eq 20)}$$
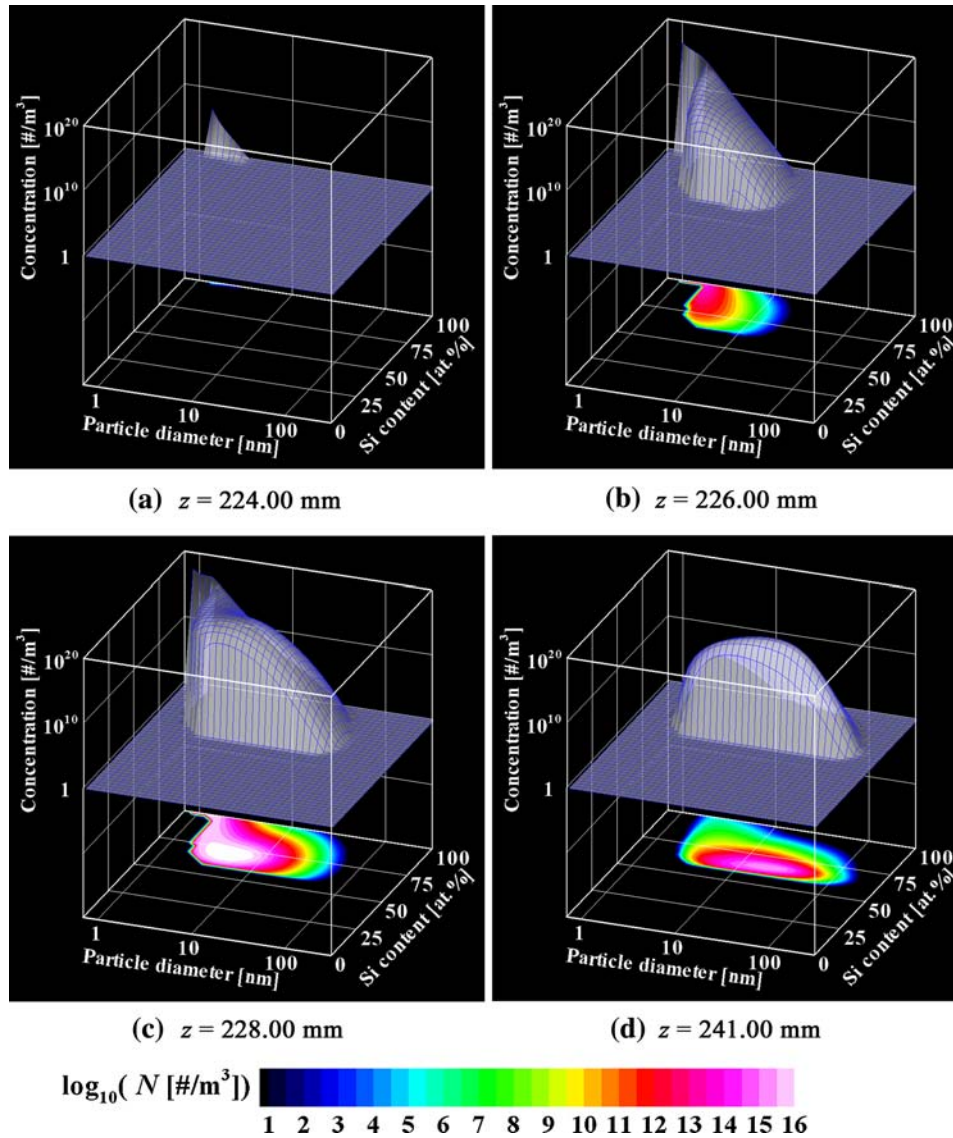
Fig. 6 Nanoparticle growth process in Ti-Si system ($\alpha_{Ti} = \alpha_{Si} = 0.05$)

Here, $A_1 = 1.257$, $A_2 = 0.4$, and $A_3 = 0.55$; μ is the gas viscosity; and Kn is the Knudsen number defined as the ratio of the gas mean free path to the particle radius.

3.3.3 Co-Condensation Process. Once stable nuclei are generated by homogeneous nucleation, supersaturated vapor heterogeneously condenses on the nuclei, resulting in significant growth of the particles. Co-condensation growth is the key process in nanoparticle formation, particularly when the vapors of two materials simultaneously become supersaturated. To evaluate this process accurately, the volume increment Δv_{i_M} of the particles at the i-th size nodes due to the condensation of material M during the infinitesimal time increment Δt is estimated by the following equation covering the entire range of Knudsen numbers (Ref 27).

$$\Delta v_{i_M} = 2\pi d_i D_{\text{vapor}_M} v_M \left(N_{\text{vapor}_M} - \bar{N}_{S_{i_M}} \right)$$
$$\times \left[\frac{0.75\alpha_M(1 + \text{Kn}_i)}{0.75\alpha_M + 0.283\alpha_M \text{Kn}_i + \text{Kn}_i + \text{Kn}_i^2} \right] \Delta t \quad \text{(Eq 21)}$$

Here, α is the accommodation coefficient that will be a key parameter in the present model. D_{vapor} represents the diffusion coefficient of the vapor estimated by Hirschfelder's formula (Ref 29). The concentration in the saturated state is modified as follows by the Kelvin effect, which is considerable for small particles (Ref 24).

$$\bar{N}_{S_{i_M}} = N_{S_M} \exp\left(\frac{4\sigma_M v_M}{d_i k_B T} \right) \quad \text{(Eq 22)}$$

The algorithm of the co-condensation process is presented in Fig. 3(c). The concept of the size-composition

splitting is analogous to the case of coagulation. All the particles at node (i, l) grow to new particles with the volume $v_i + \Delta v_{i(M=1)} + \Delta v_{i(M=2)}$ by gaining vapor during Δt. The composition (the content of material 2) of the new particles is given as

$$x'^{(cond)}_{i,j,l,m} = \frac{v_i x_l + \Delta v_{i(M=2)}}{v_i + \Delta v_{i(M=1)} + \Delta v_{i(M=2)}}. \qquad (Eq\ 23)$$

It is noted that node (i, l) becomes empty. Hence, the net production rate of condensation can be written as

$$[\dot{N}_{k,n}]_{cond} = \sum_i \sum_l \frac{(\xi^{(cond)}_{i,k} \psi^{(cond)}_{i,l,n} - \delta_{i,k}\delta_{l,n})N_{i,l}}{\Delta t}. \qquad (Eq\ 24)$$

The splitting operators in size direction ξ and in composition direction ψ are given as

and

$$\psi^{(cond)}_{i,l,n} = \begin{cases} \dfrac{x_{n+1} - x'^{(cond)}_{i,j,l,m}}{x_{n+1} - x_n}; & \text{if}\left(x_n < x'^{(cond)}_{i,j,l,m} < x_{n+1}\right) \\[2ex] \dfrac{x'^{(cond)}_{i,j,l,m} - x_{n-1}}{x_n - x_{n-1}}; & \text{if}(x_{n-1} < x'^{(cond)}_{i,j,l,m} < x_n) \\[2ex] 0; & \text{otherwise.} \end{cases} \qquad (Eq\ 26)$$

$\delta_{i,k}$ represents the Kronecker delta.

$$\delta_{i,k} = \begin{cases} 1; & \text{if}(i = k) \\ 0; & \text{if}(i \neq k) \end{cases} \qquad (Eq\ 27)$$

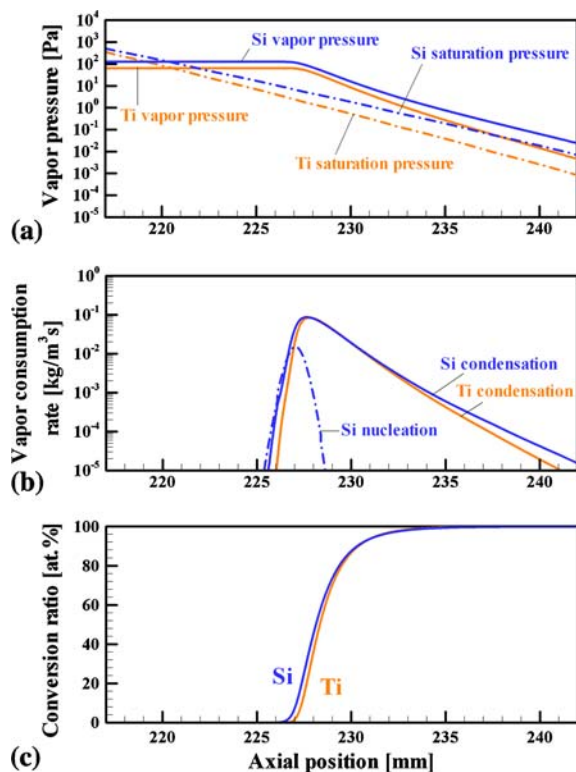**3.3.4 Monomer Balance.** To analyze the nanoparticle formation, the concentration of the monomers of the

$$\xi^{(cond)}_{i,k} = \begin{cases} \dfrac{v_{k+1} - \left(v_i + \Delta v_{i(M=1)} + \Delta v_{i(M=2)}\right)}{v_{k+1} - v_k}; & \text{if}\left(v_i < v_i + \Delta v_{i(M=1)} + \Delta v_{i(M=2)} < v_{k+1}\right) \\[2ex] \dfrac{\left(v_i + \Delta v_{i(M=1)} + \Delta v_{i(M=2)}\right) - v_{k-1}}{v_k - v_{k-1}}; & \text{if}\left(v_{k-1} < v_i + \Delta v_{i(M=1)} + \Delta v_{i(M=2)} < v_k\right) \\[2ex] 0 & \text{otherwise} \end{cases} \qquad (Eq\ 25)$$

Fig. 7 Characteristics of vapor conversion in Ti-Si system ($\alpha_{Ti} = \alpha_{Si} = 0.05$): (a) Vapor pressure, (b) vapor consumption rate, and (c) conversion ratio

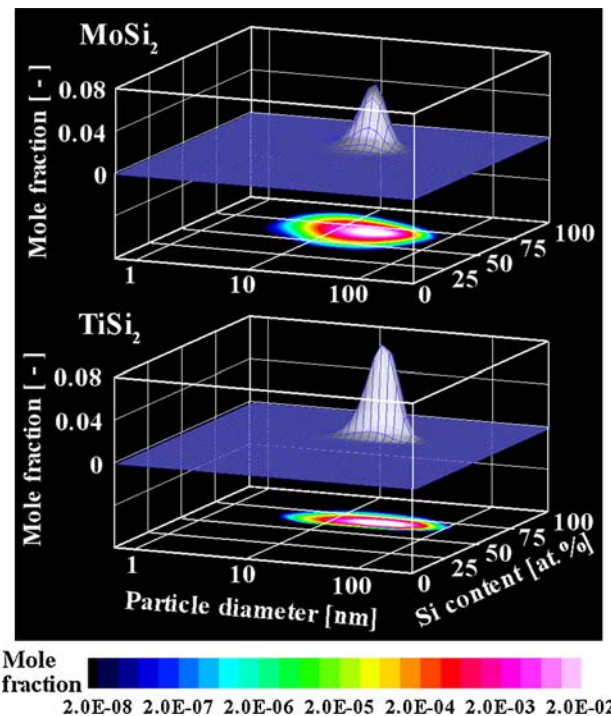**Fig. 8** Mole fractions of MoSi$_2$ and TiSi$_2$ in mature nanoparticles ($\alpha_{Mo} = \alpha_{Ti} = \alpha_{Si} = 0.05$)

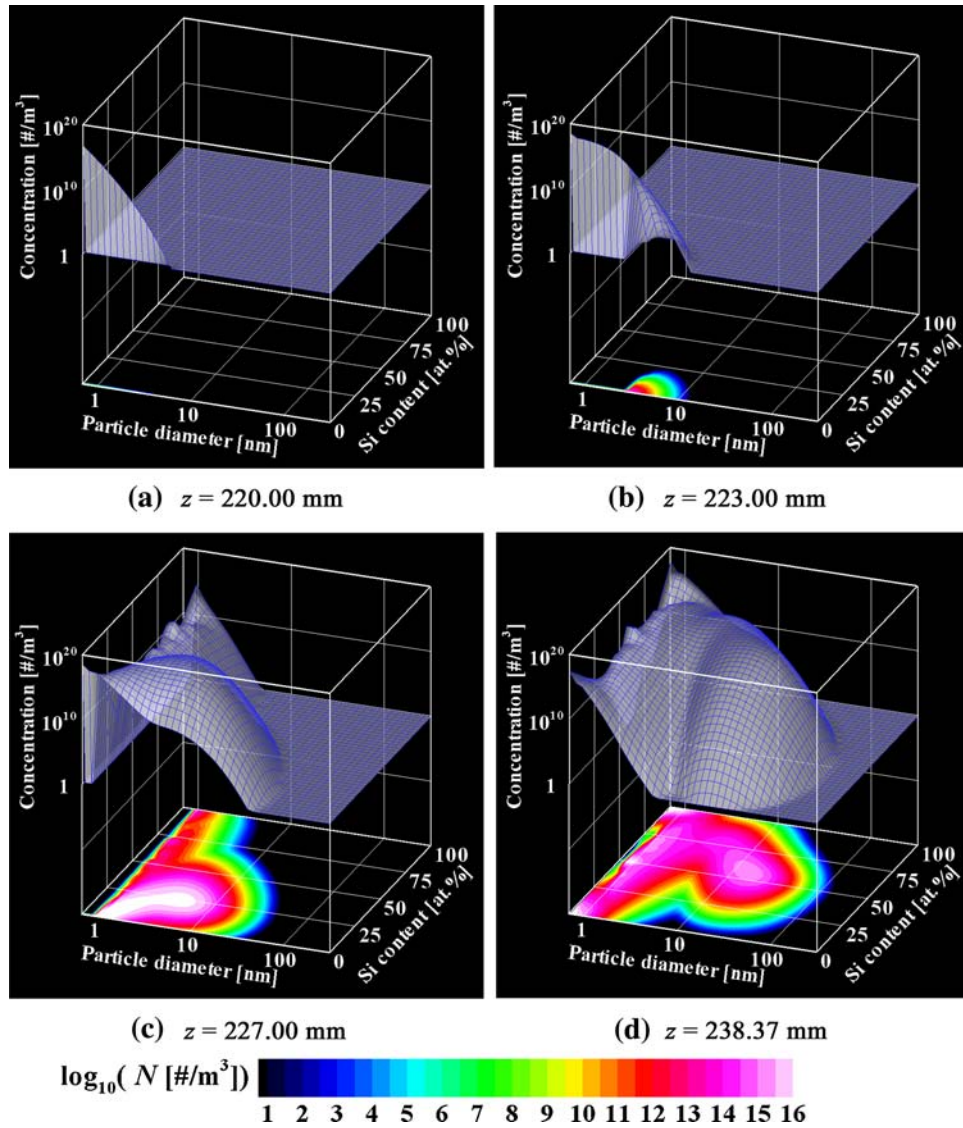**Fig. 9** Nanoparticle growth process in Mo-Si system ($\alpha_{Mo} = \alpha_{Si} = 0.01$)

material vapor must be determined simultaneously. The monomers in the gas phase are consumed by homogeneous nucleation and heterogeneous condensation.

$$\frac{dN_{vapor_M}}{dt} = \left[\dot{N}_{vapor_M}\right]_{nucl} + \left[\dot{N}_{vapor_M}\right]_{cond} \qquad \text{(Eq 28)}$$

$\left[\dot{N}_{vapor_M}\right]$ represents the net production rate of the monomers of material M. The two terms of the right-hand side have negative values for nucleation and condensation because the number of monomers is decreased by vapor consumption.

$$\left[\dot{N}_{vapor_M}\right]_{nucl} = -\sum_k I_M \xi_{kM}^{(nucl)} \frac{v_M^*}{v_M} \qquad \text{(Eq 29)}$$

$$\left[\dot{N}_{vapor_M}\right]_{cond} = -\sum_i \sum_l \frac{N_{i,l} \Delta v_{i_M}}{v_M \Delta t} \qquad \text{(Eq 30)}$$

Although Eq 29 is described in a summation, only one term remains because the nucleation supplies particles to only one node.

3.4 Computational Conditions

The computational domain is divided into finite volumes with spatial interval $\Delta z = 0.01$ mm in the axial direction. Under the target conditions, this spatial interval provides a sufficient resolution to capture the processes in nanoparticle formation, especially homogeneous nucleation, which has a much shorter characteristic time than heterogeneous condensation and coagulation. The residence time Δt is determined for every finite volume as a time step because the velocity profile is already known. The mass transfer problem with convection can thus be replaced by a simple problem in which the governing equations are calculated sequentially with each time step.

In this study, the first-order time advancement was adopted to save computational time and resources because the results were not significantly different from those obtained by the fourth-order Runge-Kutta-Gill method. The data of the bulk flow in Fig. 2 are used for the computation as mentioned in Section 2. The material properties of the metals and silicon were obtained from Ref 30 and are summarized in Table 1. The surface tension of each material depends on temperature.

4. Results and Discussion

4.1 Formation Mechanism of Silicide Nanoparticles

This section presents the computational results obtained by the present two-directional nodal model. The computations are performed for the Mo-Si system and the Ti-Si system, where the accommodation coefficients of Mo, Ti, and Si on their own silicides are all set to 0.05, i.e. $\alpha_{Mo} = \alpha_{Ti} = \alpha_{Si} = 0.05$ in Eq 21. This value is considered to be in the valid range. The effect of the accommodation coefficients will be discussed in Sections 4.2 and 4.3.

Figure 4 depicts the present computational results of the nanoparticle growth process in the Mo-Si system. Figure 5 plots the characteristics of the vapor conversion: (a) vapor pressure, (b) vapor consumption rate, and (c) conversion ratio. Pure Mo nanoparticles are growing at $z = 220$ mm in Fig. 4(a), where Mo vapor pressure is much higher than its saturation pressure and the vapor consumption rates due to nucleation and condensation are comparable (Fig. 5a, b). Both vapor consumption rates reach their maximum values at around $z = 223$ mm, where the maximum rate of condensation is approximately 10 times greater than that of nucleation. At this stage, the consumption rate of Si vapor condensation is drastically increasing as Si vapor becomes supersaturated; co-condensation growth then starts. The Si content in nanoparticles larger than 2 nm begins to increase earlier than that in the smaller nanoparticles (Fig. 4b). This is generally because vapor cannot sufficiently condense on smaller particles due to the rarefied gas effect with large Knudsen numbers in Eq 21.

At $z = 227$ mm (Fig. 4c), most of the nanoparticles have become Mo-Si compounds with increasing sizes. Figure 5(c) indicates that Mo (Si) vapor completes condensing around $z = 230$ mm (235 mm). Thus, the overall time of the co-condensation process is estimated to be 15 ms. Figure 4(d) presents the PSCD of the nanoparticles in the mature state. The majority of the nanoparticles have diameters of 10-20 nm and an Si content around 66.7 at.%, which is the stoichiometric composition of MoSi$_2$. Pure Mo nanoparticles around 1 nm still remain because they can grow efficiently by coagulation, not by condensation, with the decrease of their numbers. However, the effect of coagulation seems to be less than that of condensation in the overall growth process.

In our previous model, only one average composition could be estimated for one particle size (Ref 9). However,
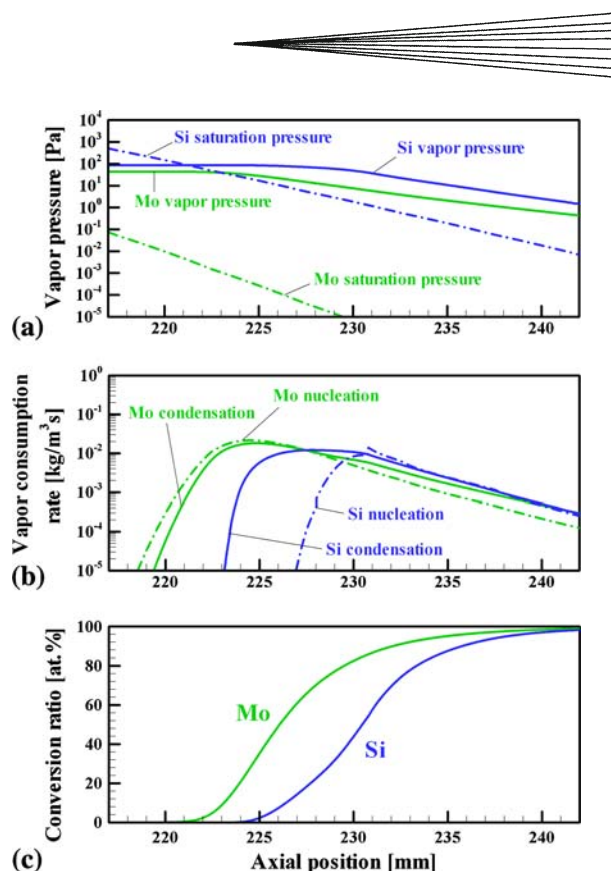

Fig. 10 Characteristics of vapor conversion in Mo-Si system ($\alpha_{Mo} = \alpha_{Si} = 0.01$): (a) Vapor pressure, (b) vapor consumption rate, and (c) conversion ratio

the present model specifies the composition distribution for the particle size of interest. For instance, in Fig. 4(d), a user can determine that 10 nm particles have an Si content distribution with a peak around 66.7 at.% and a range of 15-95 at.%. Also, it is possible to determine that the nanoparticles with an Si content of 50 at.% have a size distribution ranging from a few nanometers to 100 nm. Such ability is one of the most attractive advantages of the present two-directional nodal model.

Figure 6 depicts the computational results of the nanoparticle growth process in the Ti-Si system. Figure 7 presents the characteristics of the vapor conversion: (a) vapor pressure, (b) vapor consumption rate, and (c) conversion ratio. Figure 6(a) indicates that Si vapor first starts to nucleate around $z = 224$ mm in the Ti-Si system. Immediately after Si nucleation, Si vapor and Ti vapor simultaneously condense on Si nuclei as shown in Fig. 6(b, c) and 7(b, c). This is because the saturation vapor pressures of Ti and Si differ only slightly in Fig. 7(a). However, that difference between Mo and Si is large in Fig. 5(a). As depicted in Fig. 7(b), the vapor consumption rates reach their maximum around $z = 227$-228 mm. The maximum values of the Si and Ti condensations are approximately 10 times greater than that of Si nucleation.

The co-condensation process is almost completed around $z = 234$ mm (Fig. 7c), which means that it takes approximately 8 ms to consume both vapors. Figure 6(d) depicts the profile of the final product. The majority of the
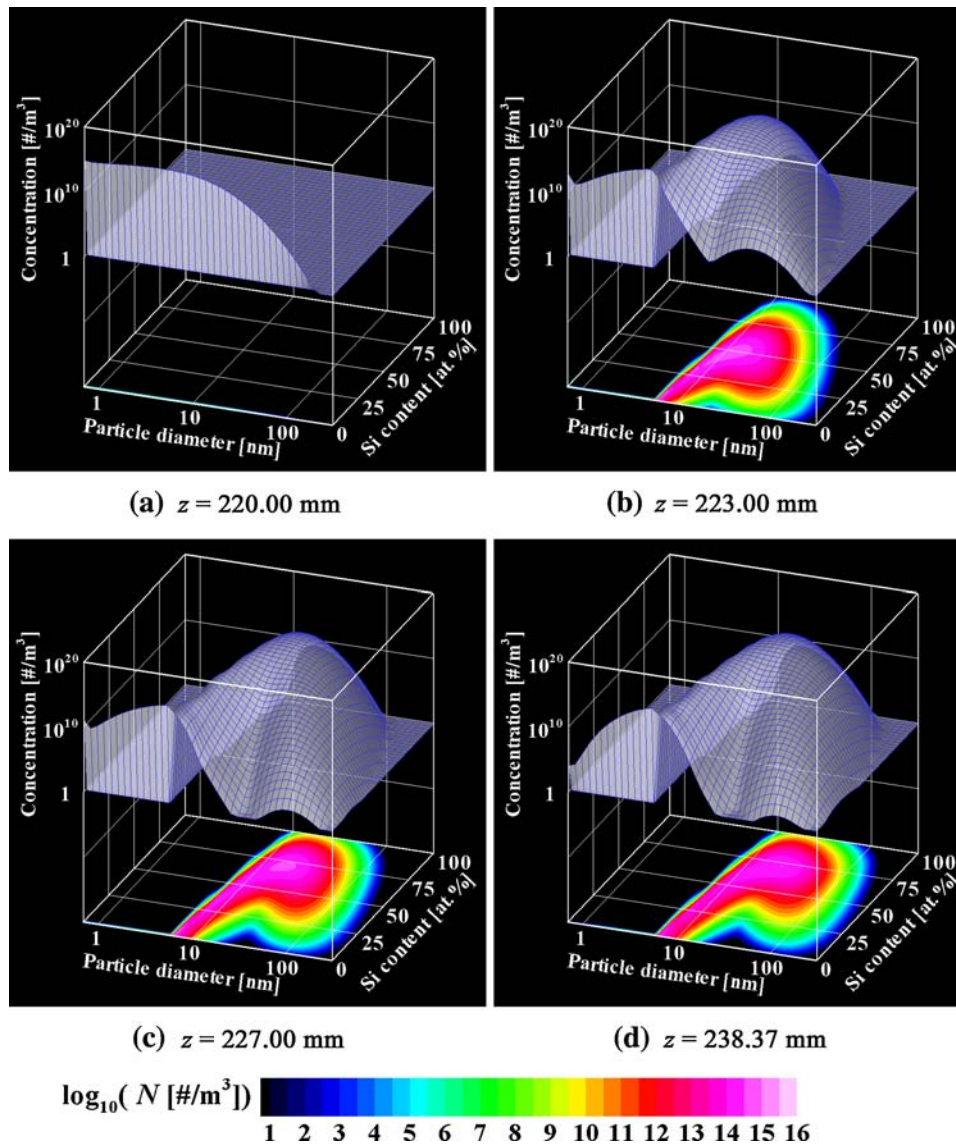
Fig. 11 Nanoparticle growth process in Mo-Si system ($\alpha_{Mo} = \alpha_{Si} = 1.0$)

nanoparticles have a near-stoichiometric composition of 60-80 at.% by virtue of the simultaneous co-condensation of two components, but no nanoparticles are produced with an Si content <60 at.%. Even such a nearly uniform composition of nanoparticles has widely ranging diameters from a few nanometers to 100 nm.

Figure 8 presents the mole fractions of $MoSi_2$ and $TiSi_2$ at each node versus the total amount of nanoparticles produced. The fractions are estimated for $MoSi_2$ at $z = 238.37$ mm and for $TiSi_2$ at $z = 241.00$ mm from their phase diagrams (Ref 25). As mentioned in Section 2, this estimation is based on the assumption that the nanoparticles stop growing at the solidification points of the disilicide obtained from the phase diagrams. Even though this is an oversimplification, it is possible to roughly estimate the compound fraction in the nanoparticle assembly under that assumption. The 10-30 nm nanoparticles have

the greatest populations of $MoSi_2$ and $TiSi_2$, and $TiSi_2$ exhibits a greater and sharper distribution than $MoSi_2$. Integrating the fractions of all the nodes, the total mole fractions of $MoSi_2$ and $TiSi_2$ in the products are calculated to be 89.8% and 92.1%. These results suggest that the initial Si content in the precursory powders should be set to 66.7 at.% to produce the disilicide nanoparticles, although the nanoparticles would not be composed of 100% disilicide.

4.2 Effect of Accommodation Coefficients

In the previous section, the accommodation coefficients are set to 0.05, which is considered to be valid because accommodation coefficients for chemical materials range from 0.013 to 0.38 around room temperature and they seem to decrease as temperature increases (Ref 27).

This section investigates the effect of the accommodation coefficients on the nanoparticle growth process predicted by the present model.

According to Eq 21, the accommodation coefficients are linked to the growth rate of a nanoparticle through heterogeneous condensation. That is, when the system has high accommodation coefficients, condensation dominates nanoparticle growth. However, condensation contributes less to nanoparticle growth when the accommodation coefficients are smaller. In that case, nucleation and/or coagulation dominate nanoparticle formation.

Figures 9 and 10 illustrate the nanoparticle growth process and the characteristics of the vapor conversion in the Mo-Si system in which both accommodation coefficients are set to 0.01, i.e. $\alpha_{Mo} = \alpha_{Si} = 0.01$. The vapor conversions are considerably slower in Fig. 10(c); consequently, Si vapor also becomes highly supersaturated (Fig. 10a). This state leads to Si nucleation even during the simultaneous co-condensation growth, as depicted in Fig. 9(c) and 10(b). As a result, the final product has an irregular distribution of particles around 1 nm in diameter (Fig. 9d). It should also be noted that the vapor consumption rate of nucleation is comparable to that of condensation (Fig. 10b).

Figures 11 and 12 also present the evolution of the nanoparticle growth and the vapor conversion process in the Mo-Si system. The accommodation coefficients of both Mo and Si are fixed to 1.0, $\alpha_{Mo} = \alpha_{Si} = 1.0$, which means that condensation dominates the nanoparticle formation process. At $z = 220$ mm, Mo nanoparticles have already grown to larger than 100 nm (Fig. 11a). Figure 12(b) indicates that the vapor consumption rates due to Mo nucleation and Mo condensation have peaks around $z = 220$ mm, and that the peak value of Mo condensation is approximately 3,000 times greater than that of Mo nucleation. Compared with Fig. 5(b) in $\alpha_{Mo} = \alpha_{Si} = 0.05$, their difference is obvious. When the accommodation coefficient is larger, a larger amount of vapor is consumed in a shorter period (Fig. 12c). In consequence, the contribution of homogeneous nucleation becomes smaller because a highly supersaturated vapor is required to obtain a high rate of homogeneous nucleation as indicated in Eq 8. This effect makes it appear as if homogeneous nucleation has been suppressed by heterogeneous condensation. In addition, Mo vapor pressure drastically drops to its saturation vapor pressure (Fig. 12a), which is also an apparent difference from Fig. 5(a).

Figure 12(b) demonstrates that the vapor consumption rate of Si condensation also increases drastically between $z = 221$ mm and $z = 222$ mm. As a result, many particles larger than 8 nm have become two-component particles at $z = 223$ mm (Fig. 11b). At $z = 227$ mm in Fig. 11(c), the PSCD has already become similar to the PSCD in Fig. 11(d), which is in the mature state. In Fig. 11(d), the peak concentration is approximately 10^{14} particles per m^3. This value is only one-tenth of the peak concentration for $\alpha_{Mo} = \alpha_{Si} = 0.05$ in Fig. 4(d). This is caused by nucleation suppression in which only a smaller number of nuclei can be generated in a condensation-dominated environment as mentioned above.
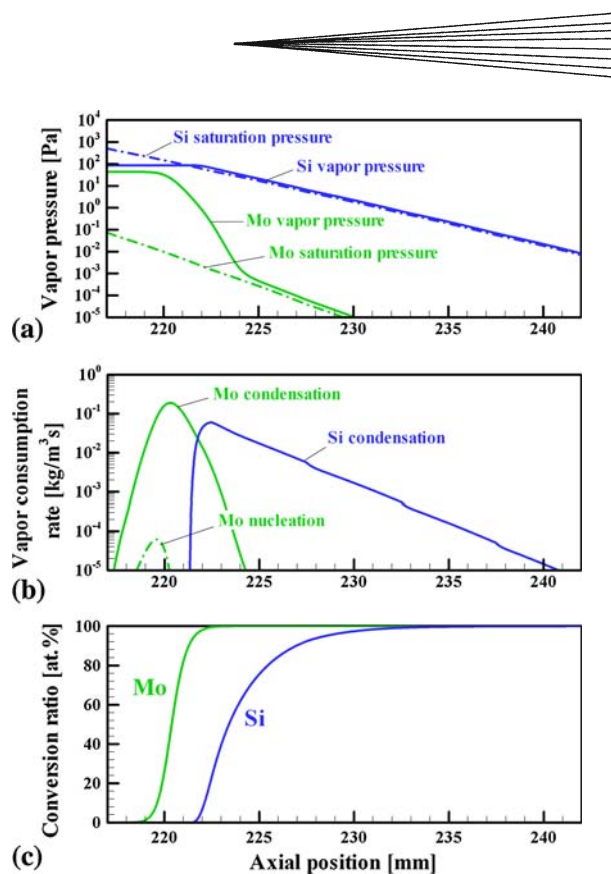

Fig. 12 Characteristics of vapor conversion in Mo-Si system ($\alpha_{Mo} = \alpha_{Si} = 1.0$): (a) Vapor pressure, (b) vapor consumption rate, (c) conversion ratio

The same discussion of the vapor conversion characteristics can be applied to a Ti-Si system, except that Si nucleation takes place first. Figures 13 and 14 illustrate the particle growth processes for $\alpha_{Ti} = \alpha_{Si} = 0.01$ and $\alpha_{Ti} = \alpha_{Si} = 1.0$. A vestige of Ti nucleation is found in Fig. 13(d). Figure 14(a) indicates that notable co-condensation has already proceeded at $z = 224$ mm. As soon as co-condensation starts, the particles promptly start to grow (Fig. 14b). After that, the PSCD does not change significantly in Fig. 14(c, d). Despite the remarkably rapid growth, the composition is almost uniform.

4.3 Verification of the Present Model

Figure 15(a, b) presents the PSD functions for the Mo-Si system and the Ti-Si system. These figures also plot the experiment results obtained from Ref 8 and 9. As mentioned in Section 2, the operating conditions of this study and those in the experiments are identical. In those experiments, the nanoparticles were collected by a ring-shaped collector at $z = 337$ mm where the nanoparticles were supposed to have already completed their growth. Because the present model concentrates nanoparticles at each node, the size distribution based on the concentration should be converted into the PSD function. In this study, the size bin for size node k is defined as

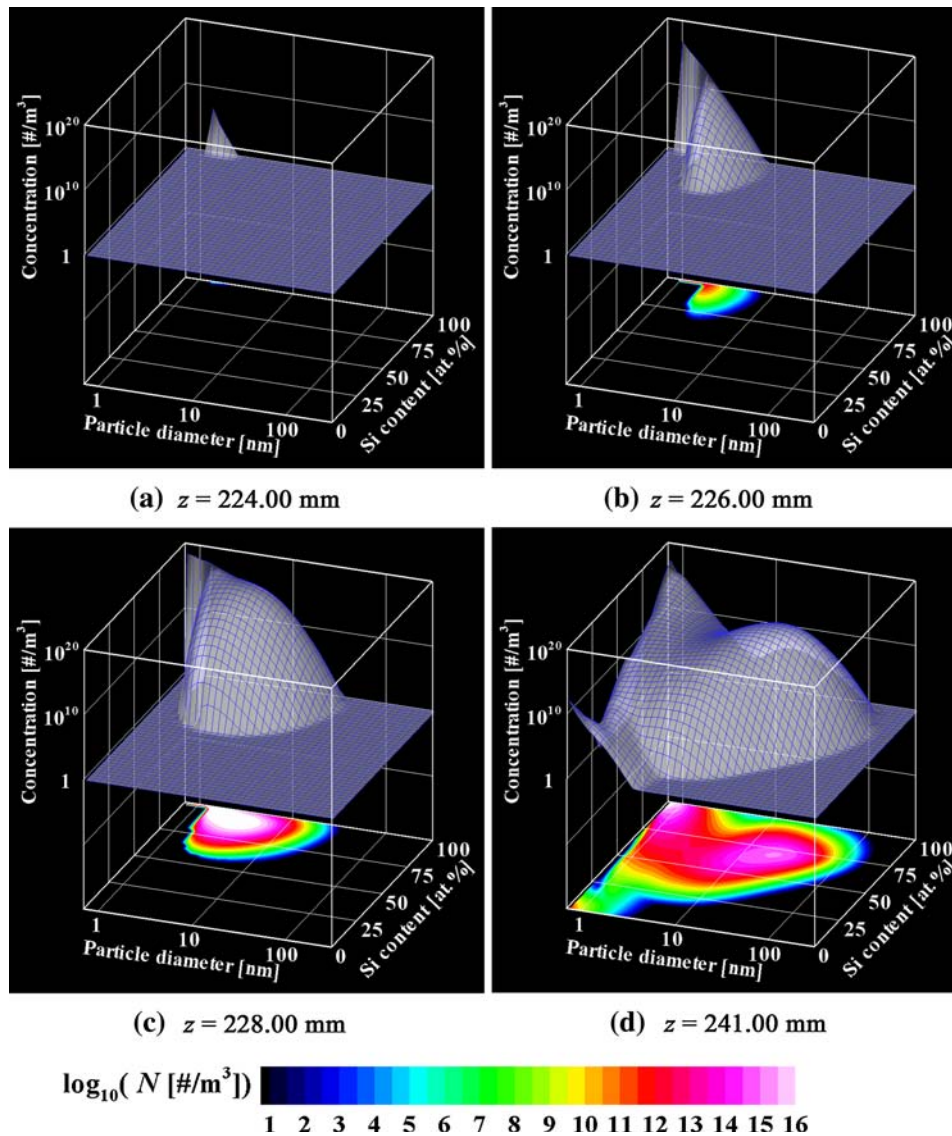$$\Delta_k = \sqrt{v_{k+1}v_k} - \sqrt{v_k v_{k-1}} \qquad \text{(Eq 31)}$$

Fig. 13 Nanoparticle growth process in Ti-Si system ($\alpha_{Ti} = \alpha_{Si} = 0.01$)

based on the logarithmic size space defined by Eq 1. The PSD function is determined by considering that this size bin includes all the nanoparticles at size node k. In both systems, the present computation results agree well quantitatively with the experiment results when the accommodation coefficients are 0.03, 0.05, and 0.1. Figure 16 illustrates the relation between the accommodation coefficients and the mole fractions of $MoSi_2$ and $TiSi_2$ estimated in the same manner used in Fig. 8. Because the present computations have been carried out in the stoichiometric condition to produce the disilicide nanoparticles, their results should indicate the maximum mole fractions. In that sense, valid composition results are also obtained when the accommodation coefficients are 0.03, 0.05, and 0.1.

These results concerning the size distribution and the composition endorse the validity of the present model,

particularly with accommodation coefficients of 0.03, 0.05, and 0.1. Furthermore, it can be concluded that the present model is ''adaptable'' because it allows a certain range of accommodation coefficients from 0.03 to 0.1. In modeling work, such adaptability is without doubt one of the greatest advantages. In addition, it has now been confirmed that setting the accommodation coefficients to 0.05 was the best selection in Section 4.1.

However, it should be mentioned that nanoparticle formation is affected by bulk conditions such as temperature and velocity. For example, as the cooling rate of the bulk flow increases, the sizes of the produced nanoparticles decrease (Ref 31). Even though the computations with accommodation coefficients of 0.05 have produced excellent results in this study, it is still unclear whether accommodation coefficients of 0.05 will always give correct answers for any condition. That is, the present model
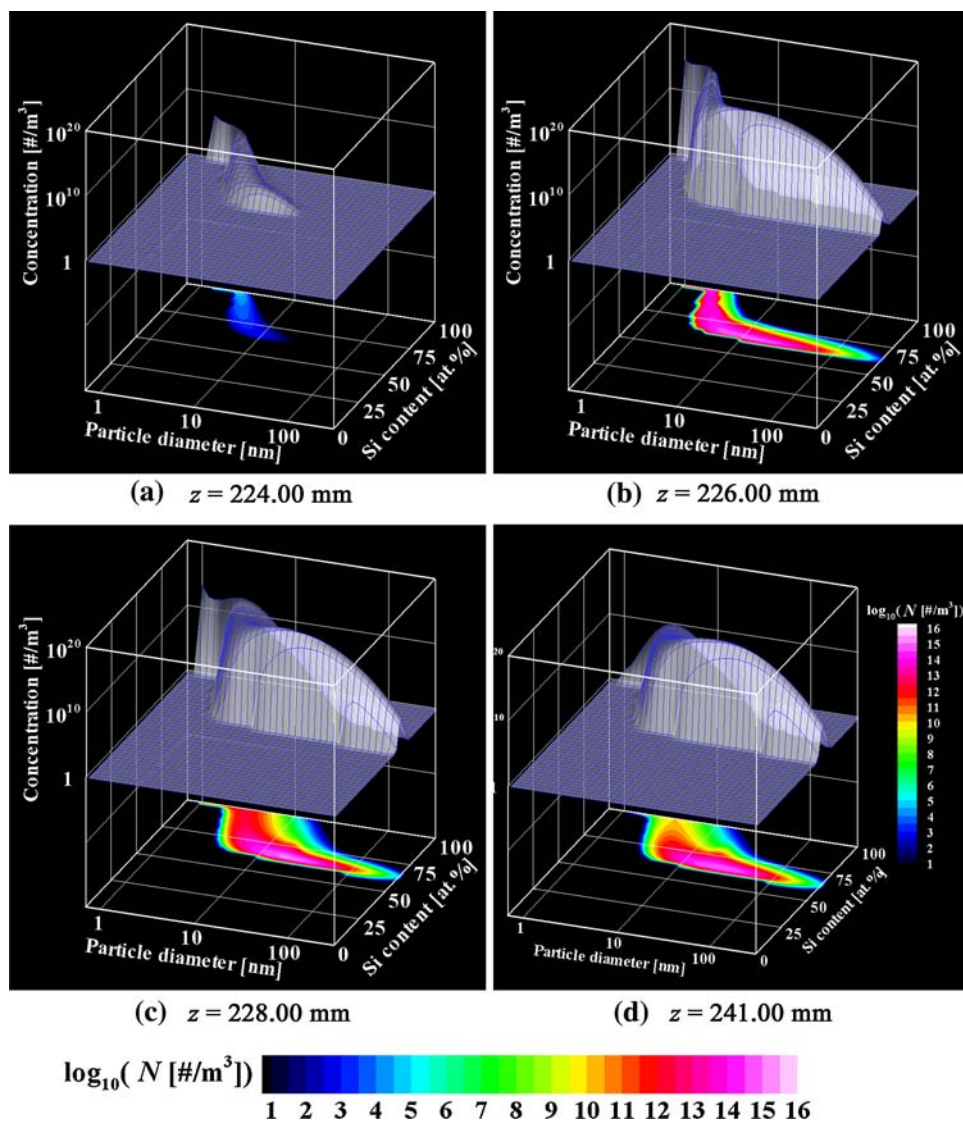
Fig. 14 Nanoparticle growth process in Ti-Si system ($\alpha_{Ti} = \alpha_{Si} = 1.0$)

includes an arbitrariness due to its accommodation coefficients. Hence, users might need to adjust the accommodation coefficients to simulate the process of interest. It is also noted that the final profiles of nanoparticles depend on the solidification point. For example, if a lower solidification point is set, the present model will predict larger nanoparticles because of the longer computation of the coagulation growth.

The present model neglected condensational heat generation and the electric charge of nanoparticles. These should be taken into account for higher accuracy because their effects possibly influence the growth process. Moreover, it should be noted that the calculations of the homogeneous nucleation rate by Eq 8 and the critical size determined by Eq 12 inherently involve errors because they adopt the surface tensions of the bulk materials. Nuclei have very small diameters of sub-nanometers, where the surface tension of the bulk material is not valid

any more. However, the data of the bulk materials have to be used because no validated data are available for small nuclei. Nevertheless, Eqs 8 and 12 are acceptable as the most reliable equations available.

In addition, it has to be mentioned that the present computation was carried out in the spatially one-dimensional domain because new models should be developed under as simple conditions as possible at first. However, actual nanoparticle formation takes place in a three-dimensional space. As a result, nanoparticles that grow in different regions will have different profiles because of different cooling rates. Furthermore, nanoparticles with different profiles diffuse, possibly merge and create a new profile. Therefore, three-dimensional computations will be required for more realistic simulation in the future.

Although such issues remain to be improved, we can conclude that the two-directional nodal model proposed in this paper is an effective tool for analyzing nanoparticle
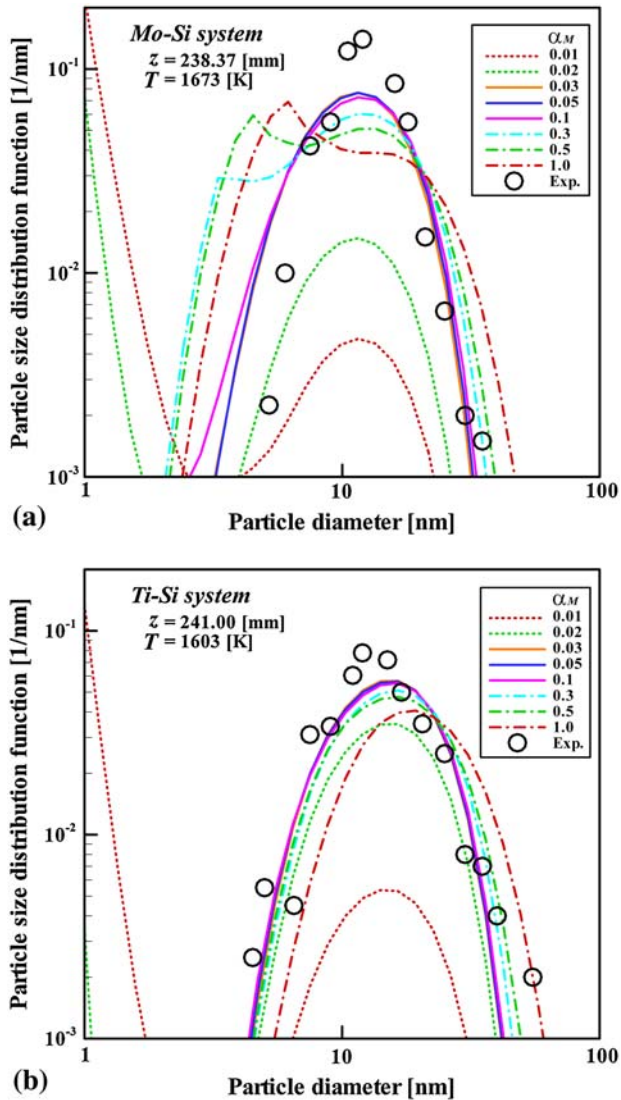
Fig. 16 Relation between the accommodation coefficient and the mole fraction: (a) MoSi$_2$ and (b) TiSi$_2$

Fig. 15 Particle size distribution functions: (a) Mo-Si system, (b) Ti-Si system (Experiment results were obtained from (a) Ref 9 and (b) Ref 8)

growth processes, including two-component co-condensation in thermal plasma processing, with sufficient accuracy.

5. Summary

A more precise but easy-to-use model has been developed and proposed to clarify nanoparticle growth with two-component co-condensation in thermal plasma processing. Computations were performed for the molybdenum-silicon and titanium-silicon systems, and the results demonstrated that the present model quantitatively estimated both the PSD and the composition distribution of the silicide nanoparticles produced through co-condensation and through nucleation and coagulation. The model also successfully obtained information that could
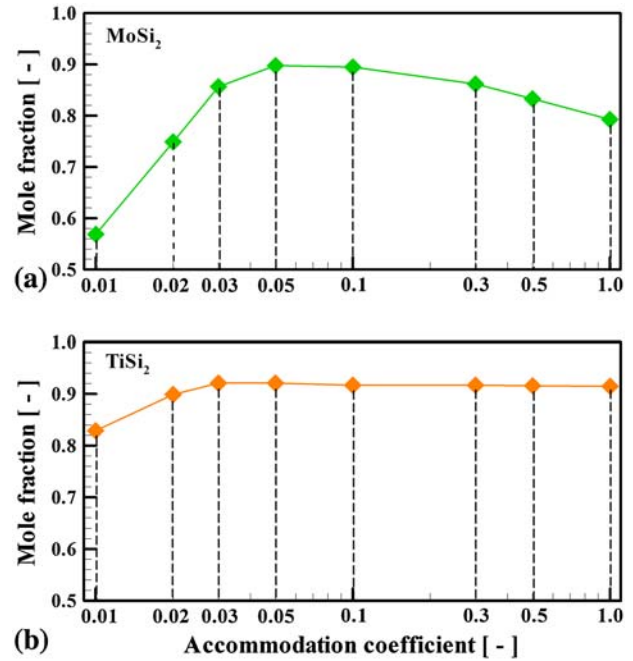
not be acquired by any other models. As a consequence, the detailed growth mechanisms of the silicide nanoparticles were revealed. We conclude that the present model is an "adaptable" and useful tool for analyzing nanoparticle growth processes, including co-condensation, with sufficient accuracy.

References

1. T. Sato, M. Shigeta, D. Kato, and H. Nishiyama, Mixing and Magnetic Effects on a Nonequilibrium Argon Plasma Jet, *Int. J. Therm. Sci.*, 2001, **40**(3), p 273-278
2. M. Shigeta, T. Sato, and H. Nishiyama, Computational Simulation of a Particle-Laden RF Inductively Coupled Plasma with Seeded Potassium, *Int. J. Heat Mass Trans.*, 2004, **47**(4), p 707-716
3. M. Shigeta and H. Nishiyama, Numerical Analysis of Metallic Nanoparticle Synthesis Using RF Inductively Coupled Plasma Flows, *Trans ASME J Heat Trans*, 2005, **127**, p 1222-1230
4. K. Matsuura, T. Hasegawa, T. Ohmi, and M. Kudoh, Synthesis of MoSi$_2$-TiSi$_2$ Pseudobinary Alloys by Reactive Sintering, *Metall. Mater. Trans. A*, 2000, **31**(3), p 747-753
5. X. Fan and T. Ishigagi, Critical Free Energy for Nucleation from the Congruent Melt of MoSi$_2$, *J. Cryst. Growth*, 1997, **171**, p 166-173
6. X. Fan, T. Ishigaki, and Y. Sato, Phase Formation in Molybdenum Disilicide Powders During In-Flight Induction Plasma Treatment, *J. Mater. Res.*, 1997, **12**(5), p 1315-1326
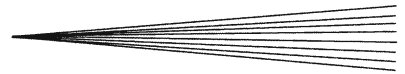
7. T. Watanabe, H. Itoh, and Y. Ishii, Preparation of Ultrafine Particles of Silicon Base Intermetallic Compound by Arc Plasma Method, *Thin Solid Films*, 2001, **390**, p 44-50

8. T. Watanabe and H. Okumiya, Formation Mechanism of Silicide Nanoparticles by Induction Thermal Plasmas, *Sci. Technol. Adv. Mater.*, 2004, **5**, p 639-646

9. M. Shigeta and T. Watanabe, Growth Mechanism of Silicon-Based Functional Nanoparticles Fabricated by Inductively Coupled Thermal Plasmas, *J. Phys. D Appl. Phys.*, 2007, **40**, p 2407-2419

10. S.L. Girshick, C.-P. Chiu, R. Muno, C.Y. Wu, L. Yang, S.K. Singh, and P.H McMurry, Thermal Plasma Synthesis of Ultrafine Iron Particles, *J. Aerosol Sci.*, 1993, **24**(3), p 367-382

11. J.F. Bilodeau and P. Proulx, A Mathematical Model for Ultrafine Iron Powder Growth in Thermal Plasma, *Aerosol Sci. Technol.*, 1996, **24**, p 175-189

12. M. Desilets, J.F. Bilodeau, and P. Proulx, Modelling of the Reactive Synthesis of Ultra-Fine Powders in a Thermal Plasma Reactor, *J. Phys. D Appl. Phys.*, 1997, **30**, p 1951-1960

13. A.C.d. Cruz and R.J. Munz, Vapor Phase Synthesis of Fine Particles, *IEEE Trans. Plasma Sci.*, 1997, **25**(5), p 1008-1016

14. A.B. Murphy, Formation of Titanium Nanoparticles from a Titanium Tetrachloride Plasma, *J. Phys. D Appl. Phys.*, 2004, **37**, p 2841-2847

15. M. Shigeta and T. Watanabe, Two-Dimensional Analysis of Nanoparticle Formation in Induction Thermal Plasmas with Counterflow Cooling, *Thin Solid Films*, 2008, **516**, p 4415-4422

16. M. Shigeta and T. Watanabe, Numerical Investigation of Cooling Effect on Platinum Nanoparticle Formation in Inductively Coupled Thermal Plasmas, *J. Appl. Phys.*, 2008, **103**, p 074903

17. N.Y.M. Gonzalez, M.E. Morsli, and P. Proulx, Production of Nanoparticles in Thermal Plasmas: A Model Including Evaporation, Nucleation, Condensation, and Fractal Aggregation, *J. Therm. Spray Technol.*, 2008, **17**(4), p 533-550

18. S.E. Pratsinis and K.-S. Kim, Particle Coagulation, Diffusion and Thermophoresis in Laminar Tube Flows, *J. Aerosol Sci.*, 1989, **20**(1), p 101-111

19. E.R. Whitby and P.H. McMurry, Modal Aerosol Dynamics Modeling, *Aerosol Sci. Technol.*, 1997, **27**, p 673-688

20. F. Gelbard, Y. Tambour, and J.H. Seifeld, Sectional Representations for Simulating Aerosol Dynamics, *J. Colloid Interf. Sci.*, 1980, **76**(2), p 541-556

21. A. Prakash, A.P. Bapat, and M.R. Zachariah, A Simple Numerical Algorithm and Software for Solution of Nucleation, Surface Growth, and Coagulation Problems, *Aerosol Sci. Technol.*, 2003, **37**, p 892-898

22. A. Vorobev, O. Zikanov, and P. Mohanty, Modelling of the In-Flight Synthesis of TaC Nanoparticles from Liquid Precursor in Thermal Plasma Jet, *J. Phys. D Appl. Phys.*, 2008, **41**, p 085-302

23. A. Vorobev, O. Zikanov, and P. Mohanty, A Co-Condensation Model for In-Flight Synthesis of Metal-Carbide Nanoparticles in Thermal Plasma Jet, *J. Therm. Spray Technol.*, 2008, **17**(5-6), p 956-965

24. S.K. Friedlander, *Smoke, Dust and Haze, Fundamentals of Aerosol Dynamics*, 2nd ed., Oxford University Press, USA, 2000

25. T.B. Massalski, *Binary Alloy Phase Diagrams*, Vol 2. American Society for Metals, Materials Park, 1990

26. S.L. Girshick, C.-P. Chiu, and P.H. McMurry, Time-Dependent Aerosol Models and Homogeneous Nucleation Rates, *Aerosol Sci. Technol.*, 1990, **13**, p 465-477

27. J.H. Seinfeld and S.N. Pandis, *Atmospheric Chemistry and Physics, From Air Pollution to Climate Change*, Wiley, New York, 1998

28. G.M. Phanse and S.E. Pratsinis, Theory for Aerosol Generation in Laminar Flow Condensers, *Aerosol Sci. Technol.*, 1989, **11**, p 100-119

29. J.O. Hirschfelder, C.F. Curtiss, and R.B Bird, *Molecular Theory of Gases and Liquids*, Wiley, New York, 1964

30. The Japan Institute of Metals, *Metal Data Book*, Maruzen, Tokyo, 1993 (in Japanese)

31. M. Shigeta, T. Watanabe, and H. Nishiyama, Numerical Investigation for Nano-Particle Synthesis in an RF Inductively Coupled Plasma, *Thin Solid Films*, 2004, **457**, p 192-200